PCCP

PAPER

View Article Online
View Journal | View Issue

Cite this: *Phys. Chem. Chem. Phys.*, 2020, **22**, 10314

Photophysical properties of the triangular $[Au(HN{=}COH)]_3$ complex and its dimer†

Jonas Greiner, [a] Rashid R. Valiev [bc] and Dage Sundholm *[d]

Received 13th March 2020,
Accepted 17th April 2020

DOI: 10.1039/d0cp01406k

rsc.li/pccp

Rate constants for radiative and non-radiative transitions of the $[Au(HN{=}COH)]_3$ complex and its dimer were calculated within the Herzberg–Teller approximation based on quantum mechanical principles. A high triplet quantum yield was estimated for the monomer. Internal conversion (IC) was found to be the major competing process to the intersystem crossing (ISC) from the lowest excited singlet state (S_1) to the lowest triplet state (T_1). ISC and IC from the spin-mixed $\tilde{T}_1$ state also dominate the triplet relaxation process resulting in a negligible phosphorescence quantum yield for the monomer. The IC and ISC rate constants of the dimer are considerably smaller due to much lower Franck–Condon factors. For the dimer a triplet quantum yield of 0.71 was estimated using the extended multi-configuration quasi-degenerate second-order perturbation theory (XMCQDPT2) method to calculate the transition energies. Fluorescence is the major competing process to the ISC relaxation of the S_1 state of the dimer. The ISC and IC processes are insignificant for the relaxation of the T_1 state, resulting in unity phosphorescence quantum yield. The high triplet and phosphorescence quantum yields of the $[Au(HN{=}COH)]_3$ dimer make it and its higher oligomers potential candidates as dopants for phosphorescent organic light emitting diodes and as down-converters in solid-state lighting systems.

1 Introduction

The incorporation of gold atoms into organic molecules to form organogold compounds has lead to many interesting structures that have been studied experimentally and theoretically for their optical properties and their ability to form metallophilic bonds.[1–17] Many organogold complexes exhibit high intensity and short phosphorescence lifetime at room temperature.[6,7,9,18] Therefore, compounds such as the trinuclear gold(I) carbeniate complexes $[Au(RN{=}COR')]_3$ studied in this work are of considerable interest due to their optoelectronic properties. Gold(I) complexes are often able to form intermolecular bonds energetically comparable to hydrogen bonds that are based on strong aurophilic interactions.[11,19–21] These interactions influence the solid state structures and are strong enough to affect the properties of the molecules in solution.[22–25] Due to these interactions $[Au(RN{=}COR')]_3$ complexes can assemble into dimers, trimers and oligomers and form extended chains in the solid state.[18,26–30]

The $[Au(HN{=}COH)]_3$ compound studied in this work has to our knowledge not been synthesized. Therefore there are no comparable experimental properties available. However, $[Au(HN{=}COH)]_3$ can be treated as a model system for the $[Au(RN{=}COR')]_3$ group of compounds. The prominent example for this structure is $[Au(MeN{=}COMe)]_3$, first synthesized by Minghetti *et al.*[31] There has been much experimental and computational investigation into this compound, especially concerning its solvoluminescent properties.[18,26–29,32–37] After irradiating the hexagonal crystals of this compound with near-UV light and adding a drop of solvent a bright yellow flash can be observed.[26,32] This solvoluminescence has been explained by the excitation of $[Au(MeN{=}COMe)]_3$ in the solid state resulting in luminescence emission from dimers in the solution.[37] Better solvents for this compound lead to higher luminescence intensity.[33] In its solid state $[Au(MeN{=}COMe)]_3$ exhibits white light emission in the visible region (400 nm to 700 nm) which has been explained through the combination of two bands: a blue band that results from the solid state band gap and leads to a contraction of the intermolecular Au–Au-distances upon excitation and an orange-red band that arises from trapped excitons within the disordered stacks of the structure.[18] Crystallized needles of $[Au(MeN{=}COMe)]_3$ have also been used as a molecular nanowire to fabricate p-type semiconductors in an organic field transistor.[18]

[a] *Institut für Physikalische Chemie, Johannes Gutenberg-Universität Mainz, Duesbergweg 10-14, D-55128 Mainz, Germany. E-mail: jgreiner@students.uni-mainz.de*
[b] *Institute for Atmospheric and Earth System Research, Faculty of Science, FIN-00014 University of Helsinki, Finland. E-mail: valievrashid@gmail.com*
[c] *Tomsk State University, Lenin Avenue 36, Tomsk 634050, Russia*
[d] *Department of Chemistry, Faculty of Science, P.O. Box 55 (A.I. Virtanens plats 1), FIN-00014 University of Helsinki, Finland. E-mail: Dage.Sundholm@helsinki.fi*

† Electronic supplementary information (ESI) available: The Cartesian ground and excited state coordinates of the optimized molecular structures are available free of charge. See DOI: 10.1039/d0cp01406k

[Au(MeN=COMe)]$_3$ could be of interest for diode lighting applications due to its broad white light emission. The white color produced by one phosphor is not susceptible to visual discoloration effects over the diodes lifespan, which is problematic when mixing the colors of multiple fluorophors or phosphors with different lifetimes.[18] Therefore, this phosphor could be used as a down-converter in conjunction with regular light emitting diodes (LEDs) or organic light emitting diodes (OLEDs).[38,39] Due to their high phosphorescence intensity in the solid state, gold(I) carbeniate complexes are also possible candidates as dopants in phosphorescent organic light emitting diodes (PhOLEDs).[38,40] These potential applications validate an investigation into the energies, kinetics and lifetimes of the electronic states of these systems. Efficient PhOLED applications require short phosphorescence lifetimes and large intersystem crossing (ISC) rates to ensure that both triplet and singlet excitons generated through charge injection are utilized effectively for visible light emission. This would yield near 100% quantum efficiency that could potentially reduce the power consumption by 75% compared to high quantum yield fluorescent OLEDs.[38,40] The ability to transform singlet excitons into triplet excitons through ISC is even more important for down-conversion phosphor applications as this method solely produces singlet excited states.[39]

The phosphorescence quantum yield is obtained as[41,42]

$$\phi_{\text{phos}} = \frac{k_{\text{phos}}}{k_{\text{phos}} + k_{\text{IC}} + k_{\text{ISC}}} \tag{1}$$

where k_{phos} is the rate constant of the phosphorescence, k_{IC} is the rate constant for internal conversion (IC), and k_{ISC} is the one for the ISC process. The triplet quantum yield

$$\phi_{\text{T}} = \frac{k_{\text{ISC}}}{k_{\text{ISC}} + k_{\text{IC}} + k_{\text{r}}} \tag{2}$$

can be analogously calculated from the radiative rate constant (k_{r}) of fluorescence and the non-radiative (k_{ISC} and k_{IC}) rate constants. The rate constants of non-radiative transitions such as the ISC and IC rates are experimentally difficult to access. Computational studies make estimates of these rate constants on the basis of quantum mechanical principles possible.[43,44]

The fluorescence rate from state S_1 can be approximated from oscillator strengths using the Strickler–Berg equation.[45] Spin–orbit coupling has to be considered for transition processes between states of different multiplicity such as ISC and phosphorescence. Instead of using the exact two-component or the Breit-Pauli-Hamiltonian the spin–orbit coupling can be approximated as an effective one-electron operator ($\hat{H}_{\text{SO}}$). This operator can be treated as a perturbation if the spin–orbit coupling is small compared to the transition energy of the involved states, which was found to be true for all systems treated in this work. The lifetime and phosphorescence rate of the triplet state can be calculated from the transition strengths.[46] The non-radiative transition rate constants are calculated using a method developed by Valiev *et al.*,[43,44] where the expression for the rate constant of internal conversion is

$$k_{\text{IC}} = \frac{4}{\Gamma_{\text{f}}} \sum_{n_1,n_2,\ldots,n_{3N-6}}^{\text{Comb}} \left(D \prod_{k=1}^{3N-6} \left(\frac{\mathrm{e}^{-y_k} y_k^{n_k}}{n_k!} \right)^{\frac{1}{2}} + \sum_{j=1}^{3N-6} d_j b_j \times \prod_{\substack{k=1 \\ k\neq j}}^{3N-6} \left(\frac{\mathrm{e}^{-y_k} y_k^{n_k}}{n_k!} \right)^{\frac{1}{2}} + \sum_{\substack{j=1 \\ j'=1}}^{3N-6} b_j t_{j'} W_{jj'} \prod_{\substack{k=1 \\ k\neq j \\ k\neq j'}}^{3N-6} \left(\frac{\mathrm{e}^{-y_k} y_k^{n_k}}{n_k!} \right)^{\frac{1}{2}} \right)^2, \tag{3}$$

where Γ_{f} is the line width. The Comb summation runs over those linear combinations of vibrational frequencies that add up to the electronic transition energy $E_{\text{if}} = n_1\omega_1 + n_2\omega_2 + \ldots + n_{3N-6}\omega_{3N-6}$, where n_k is the excitation level of the kth vibrational mode. This ensures that the energy conservation is fulfilled during the transition. All linear combinations within a margin of 200 cm^{-1} of E_{if} are taken into account. The corresponding expression for calculating the rate constant for intersystem crossing is

$$k_{\text{ISC}} = \frac{4}{\Gamma_{\text{f}}} \sum_{n_1,n_2,\ldots,n_{3N-6}}^{\text{Comb}} \left(\langle \phi_{\text{i}}(\mathbf{r},\mathbf{s},\mathbf{R}) | \hat{H}_{\text{SO}} | \phi_{\text{f}}(\mathbf{r},\mathbf{s},\mathbf{R}) \rangle \big|_{\mathbf{R}=\mathbf{R}_0} \times \prod_{k=1}^{3N-6} \left(\frac{\mathrm{e}^{-y_k} y_k^{n_k}}{n_k!} \right)^{\frac{1}{2}} + \sum_{j=1}^{3N-6} t_j W_j \prod_{\substack{k=1 \\ k\neq j}}^{3N-6} \left(\frac{\mathrm{e}^{-y_k} y_k^{n_k}}{n_k!} \right)^{\frac{1}{2}} \right)^2, \tag{4}$$

where $\phi_{\text{i}}(\mathbf{r},\mathbf{s},\mathbf{R})$ and $\phi_{\text{f}}(\mathbf{r},\mathbf{s},\mathbf{R})$ are the initial and final electronic states. $\mathbf{r}$ and $\mathbf{s}$ denote electronic space and spin coordinates. The spin–orbit coupling element is calculated at the equilibrium geometry $\mathbf{R} = \mathbf{R}_0$ of the initial electronic state. The rest of the terms in eqn (3) and (4) are given by

$$D = -\sum_{\nu}\sum_{q} \frac{1}{2M_\nu} \left\langle \phi_{\text{i}}(\mathbf{r},\mathbf{s},\mathbf{R}) \left| \frac{\partial^2}{\partial R_{q\nu}^2} \right| \phi_{\text{f}}(\mathbf{r},\mathbf{s},\mathbf{R}) \right\rangle \Big|_{\mathbf{R}=\mathbf{R}_0}$$

$$d_j = -\sum_{\nu}\sum_{q} \frac{L_{\nu qj}}{\sqrt{M_\nu}} \left\langle \phi_{\text{i}}(\mathbf{r},\mathbf{s},\mathbf{R}) \left| \frac{\partial}{\partial R_{q\nu}} \right| \phi_{\text{f}}(\mathbf{r},\mathbf{s},\mathbf{R}) \right\rangle \Big|_{\mathbf{R}=\mathbf{R}_0}$$

$$b_j = \left\langle \chi_{\text{i}0_j}(Q_j) \left| \frac{\partial}{\partial Q_j} \right| \chi_{\text{f}n_j}(Q_j) \right\rangle = \sqrt{\frac{1}{2n_j!}\omega_j (n_j - y_j)^2 \mathrm{e}^{-y_j} y_j^{n_j - 1}}$$

$$t_j = \left\langle \chi_{\text{i}0_j}(Q_j) | Q_j | \chi_{\text{f}n_j}(Q_j) \right\rangle = \sqrt{\frac{1}{2\omega_j n_j!}(n_j + y_j)^2 \mathrm{e}^{-y_j} y_j^{n_j - 1}}$$

$$W_{jj'} = -\sum_{\nu,\nu'}\sum_{q,q'} \frac{L_{\nu qj} L_{\nu' q' j'}}{\sqrt{M_\nu M_{\nu'}}} \left\langle \phi_{\text{i}}(\mathbf{r},\mathbf{s},\mathbf{R}) \left| \frac{\partial^2}{\partial R_{q\nu} \partial R_{q'\nu'}} \right| \phi_{\text{f}}(\mathbf{r},\mathbf{s},\mathbf{R}) \right\rangle \Big|_{\mathbf{R}=\mathbf{R}_0}$$

$$W_j = \sum_{\nu}\sum_{q} \frac{L_{\nu qj}}{\sqrt{M_\nu}} \frac{\partial}{\partial R_{\nu q}} \langle \phi_{\text{i}}(\mathbf{r},\mathbf{s},\mathbf{R}) | \hat{H}_{\text{SO}} | \phi_{\text{f}}(\mathbf{r},\mathbf{s},\mathbf{R}) \rangle \big|_{\mathbf{R}=\mathbf{R}_0}, \tag{5}$$

where M_ν is mass of ν-th nucleus and $q = x,y,z$. χ denotes the nuclear wave functions in the harmonic approximation. The

integrals of the nuclear wave function have been transformed into normal coordinates Q_j using $R_{\nu q} - R_{0\nu q} = M_\nu^{-1/2} L_{\nu q j} Q_j$, where $L_{\nu q j}$ is the linear relation between the Cartesian and normal coordinates. These integrals including Franck–Condon factors are written in terms of Huang–Rhys factors:

$$y_j = \frac{1}{2}\omega_j \left| Q_{0_j}^{\mathrm{f}} - Q_{0_j}^{\mathrm{i}} \right|^2, \quad (6)$$

where ω_j is the vibrational frequency of mode j. Matrix elements of the non-adiabatic coupling operator $\frac{\partial^2}{\partial \mathbf{R}^2}$ and the electronic wave functions are needed for calculation of k_{IC} between S_1 and S_0. Matrix elements of the spin–orbit coupling operator and the electronic wave functions are needed for calculation of k_{ISC} between S_1 and T_1 and between T_1 and S_0.

Spin–orbit coupling between the triplet state T_1 and the singlet states of the system leads to a spin-mixed $\tilde{T}_1$ state. IC from $\tilde{T}_1$ to S_0 is possible and is another process that competes with the phosphorescence and ISC transition from T_1.[47,48]

2 Computational methods

Density functional theory (DFT) optimizations of the ground and excited state molecular structures and calculations of the vibrational frequencies were carried out with Turbomole[49–52] using the Karlsruhe triple-zeta basis set augmented with a double set of polarization functions (def2-TZVPP),[53,54] the B3-LYP functional[55–57] and the m5 integration grid.[58] No symmetry constraints were imposed. The 60 inner electrons of the gold atoms were replaced by an effective core-potential (ECP) to consider scalar relativistic effects and to reduce computational costs.[59] Dispersion corrections have to be taken into account to describe gold–gold interactions accurately. The D3-BJ dispersion correction was used in all DFT calculations.[60] The optimized ground state molecular structures are shown in Fig. 1. The singlet excited state geometries were optimized using the time-dependent DFT (TD-DFT) method using the B3-LYP functional.[55–57,61–64] The molecular structures of the lowest triplet state were calculated using unrestricted ground state DFT with a triplet occupation.[51]

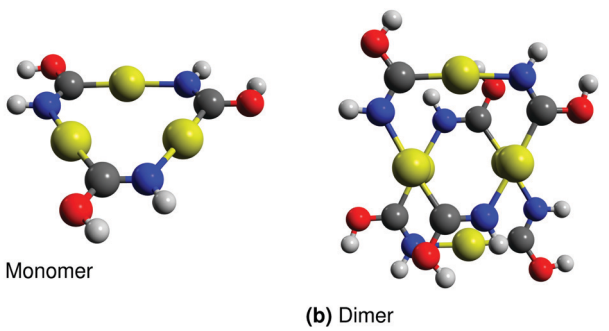

Fig. 1 Molecular ground state structures of the studied molecules. H in white, C in grey, N in blue, O in red and Au in yellow. The graphics were created using Avogadro.[65,66]

The ground state vibrational frequencies were calculated from the analytic second derivative of the energy using the AOFORCE module.[67,68] The second derivatives of the excited states of the molecules were calculated numerically from the analytical gradients using the NUMFORCE module.

The excitation energies and oscillator strengths were calculated using the molecular structures optimized at the DFT and TD-DFT levels. We employed TD-DFT calculations[61,62,64] and second-order approximate coupled-cluster theory (CC2) calculations using the resolution-of-the-identity approximation[69,70] implemented in the Turbomole program[49,50,52] as well as calculations at the extended multi-configuration quasi-degenerate second-order perturbation theory (XMCQDPT2) level[71] implemented in the Firefly program.[72] This procedure was chosen because the involved states may exhibit multireference character and because accurate excitation energies are needed for the calculation of rate constants. Active spaces consisting of 12 electrons in 12 molecular orbitals and 8 electrons in 9 molecular orbitals were chosen in the multireference calculations of the monomer and the dimer, respectively.

The non-adiabatic coupling matrix elements[73] were calculated with Turbomole at the TD-DFT level using the S_1 geometry.[49,50,52] The spin–orbit coupling (SOC) matrix elements[74] were computed with GAMESS-US[75,76] at the complete active space self-consistent field (CAS-SCF) level using the full Breit-Pauli spin–orbit operator. The molecular structures of the S_1 and T_1 states were used in the SOC calculations.

The fluorescence rates (k_{r}) were obtained from the oscillator strengths using the Strickler–Berg equation.[45] The phosphorescence rates (k_{phos}) were calculated using perturbation theory (PT) with Turbomole[49,50,52] at the SOC-PT-CC2 level[46] using the TD-DFT geometries. The IC and ISC rate constants (k_{IC} and k_{ISC}) were calculated within the Herzberg–Teller approximation[77] using the methodology developed by Valiev *et al.*[43,44] The IC rate constant from the $\tilde{T}_1$ state to the S_0 ground state was calculated from the state mixing coefficients and the excitation energies using the formula by Artyukhov *et al.*[47,48]

3 Results and discussion

3.1 Monomer

The ground state of the $[Au(HN{=}COH)]_3$ complex is a planar molecule belonging to the C_{3h} point group. The lowest excited singlet and triplet states break the planar symmetry of the ground state by moving an OH group and a NH group out of the plane. Two enantiomers are possible due to the chiral nature of the molecular structure of the excited states. The optimized ground and excited state structures of the $[Au(HN{=}COH)]_3$ complex are shown in Fig. 2. The vertical excitation energies calculated for the molecular structure of the excited states of the monomer at the TD-DFT, CC2 and XMCQDPT2 levels are reported in Table 1.

The de-excitation energies for the $S_1 \rightarrow S_0$ transition calculated at the three levels of theory agree within 0.12 eV, whereas the calculated values for the transition energy from the lowest triplet state (T_1) to S_0 calculated at the B3-LYP level is 0.4 eV smaller than the XMCQDPT2 value. The phosphorescence

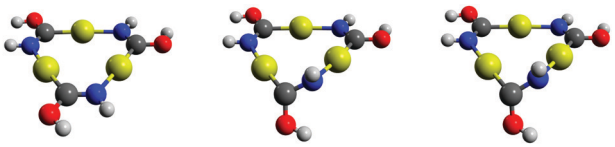

Fig. 2 The molecular structures of the lowest electronic states of the $[Au(HN{=}COH)]_3$ complex. H in white, C in grey, N in blue, O in red and Au in yellow. The graphics were created using Avogadro.[65,66]

Table 1 Transition energies in cm^{-1} (eV) of the S_0, S_1 and T_1 states of the $[Au(HN{=}COH)]_3$ complex at the respective equilibrium geometries of the excited state calculated at the TD-DFT, CC2 and XMCQDPT2 levels

Structure	Transition	TD-DFT	CC2	XMCQDPT2
S_0	$S_0 \rightarrow S_1$	38 741 (4.803)	43 224 (5.359)	42 100 (5.220)
S_1	$S_1 \rightarrow S_0$	16 197 (2.008)	15 973 (1.980)	16 939 (2.100)
T_1	$T_1 \rightarrow S_0$	11 333 (1.405)	12 448 (1.543)	14 503 (1.798)

energy of the T_1 state calculated at the CC2 level is 0.25 eV smaller than obtained in the XMCQDPT2 calculation. The differences between the singlet and triplet excitation energies calculated at the B3-LYP, CC2, and XMCQDPT2 levels using the S_1 geometry are 0.247, 0.122, and 0.186 eV, respectively. B3-LYP has a tendency to underestimate excitation energies of triplet states,[78] whereas a comprehensive benchmark study showed that CC2 triplet energies are in good agreement with reference data.[79] It is not elucidated whether the excitation energies calculated at the CC2 or the XMCQDPT2 level are more accurate, since XMCQDPT2 excitation energies have never been properly benchmarked. However, the employed multi-state XMCQDPT2 approach is expected to treat the excited states in a more balanced manner than low-order single-reference methods implying that the energy difference between the S_1 and T_1 states is most likely more accurate at the XMCQDPT2 level than obtained in the CC2 calculations.

A very large Stokes shift of more than 2.7 eV was obtained using all three methods, which can be attributed to the differences in the equilibrium structures of the ground state and the excited states. The molecular structures of the singlet and triplet excited states as well as their excitation energies are similar, which means that little vibrational relaxation is necessary for the ISC process from S_1 to T_1. The $[Au(MeN{=}COMe)]_3$ molecule absorbs light in the UV region and emits between 400 nm and 450 nm in chloroform solution.[18,26,32] The fact that the calculated de-excitation energies are much smaller than the experimental emission energies suggests that the monomer is not the emitting species in solution.

Photophysical properties have also been calculated at the different levels of theory. The calculated oscillator strengths, spin–orbit coupling matrix elements and phosphorescence lifetimes at their respective level of theory are presented in Table 2. The radiative and non-radiative rate constants were calculated using both CC2 and XMCQDPT2 transition energies. The phosphorescence lifetime was only calculated at the CC2 level. The obtained results are presented in Table 3.

Table 2 Oscillator strength ($f(S_1 \rightarrow S_0)$), spin–orbit coupling matrix elements ($\langle S_1|\hat{H}_{SO}|T_1\rangle$ and $\langle T_1|\hat{H}_{SO}|S_0\rangle$) and phosphorescence lifetime (τ) of the $[Au(HN{=}COH)]_3$ complex calculated at the given levels of theory

$f(S_1 \rightarrow S_0)$		$\langle S_1\|\hat{H}_{SO}\|T_1\rangle$	$\langle T_1\|\hat{H}_{SO}\|S_0\rangle$	τ
CC2	XMCQDPT2	CAS-SCF	CAS-SCF	CC2
0.003	0.003	4 cm^{-1}	28 cm^{-1}	0.13

Table 3 The rate constants of the fluorescence (k_r) and phosphorescence (k_{phos}) transitions as well as the rate constants of the non-radiative transitions (k_{IC} and k_{ISC}) between the lowest singlet (S_0 and S_1) and triplet (T_1) states of the $[Au(HN{=}COH)]_3$ complex calculated at the CC2 and XMCQDPT2 levels of theory

Level	k_r	k_{IC}	k_{ISC}	k_{phos}
$S_1 \rightarrow S_0$				
CC2	5×10^5 s^{-1}	2×10^{10} s^{-1}		
XMCQDPT2	5×10^5 s^{-1}	7×10^9 s^{-1}		
$S_1 \rightarrow T_1$				
CC2			3×10^{10} s^{-1}	
XMCQDPT2			2×10^{10} s^{-1}	
$T_1 \rightarrow S_0$				
CC2		2×10^3 s^{-1}	1×10^4 s^{-1}	8 s^{-1}
XMCQDPT2		2×10^3 s^{-1}	8×10^3 s^{-1}	—

The strong spin–orbit coupling between S_1 and T_1 and the large Franck–Condon factors of the $S_1 \rightarrow T_1$ transition are responsible for the fast ISC rate, which leads to large triplet quantum yields. The Franck–Condon factors are large, because high-energy vibrational modes have significant vibronic coupling due to small differences in the molecular structures of the two excited states. The small energy gap between S_1 and T_1 also leads to large Franck–Condon factors, because only low excitations of the vibrational modes are needed to fulfill the energy conservation condition of the transition.

The IC from S_1 to S_0 is the main competing process to ISC, even though the energy difference between S_1 and S_0 is much larger than between S_1 and T_1. Large Franck–Condon factors were obtained for the $S_1 \rightarrow S_0$ transition due to a strong non-adiabatic coupling, which results in a large rate constant for the IC process.

Fluorescence from S_1 is insignificant because the oscillator strength between S_1 and S_0 is very small. A slow phosphorescence rate was obtained for the monomer, which leads to a long phosphorescence lifetime of 0.13. Strong spin–orbit and vibronic coupling between T_1 and S_0 cause the ISC and IC processes from the spin-mixed $\tilde{T}_1$ state to dominate the triplet relaxation process resulting in a negligible phosphorescence quantum yield.

The results calculated at the CC2 and XMCQDPT2 levels are quite similar. The very small differences in the IC and ISC rate constants obtained at the two levels stem from the similar energy differences reported in Table 1. The XMCQDPT2 calculations yield larger energy gaps as well as smaller k_{ISC} and k_{IC} rate constants. A larger number of combined vibrational transitions is therefore necessary to fulfill the energy conservation condition, which leads to smaller Franck–Condon factors and

Table 4 Triplet and phosphorescence quantum yields ϕ_T and ϕ_{phos} of the $[Au(HN{=}COH)]_3$ complex calculated at the CC2 and XMCQDPT2 levels

Level	ϕ_T	ϕ_{phos}
CC2	0.60	0.0007
XMCQDPT2	0.74	0.0007

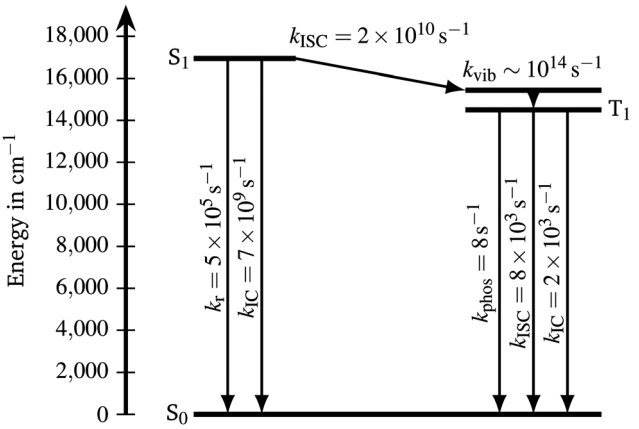

Fig. 3 The Jablonski diagram of the $[Au(HN{=}COH)]_3$ complex calculated at the XMCQDPT2 level.

slower IC and ISC rates. The larger k_{ISC}/k_{IC} ratio obtained in the XMCQDPT2 calculations leads to a slightly larger triplet quantum yield. The calculated triplet and phosphorescence quantum yields are reported in Table 4. The rate constants calculated at the XMCQDPT2 level are summarized in the Jablonski diagram in Fig. 3.

The monomer is not suitable for optoelectronic applications because non-radiative transitions dominate the relaxation of the singlet and triplet excited states. Comparison of excitation energies and prior research also suggest that the monomer is neither the emitting species in the solution nor in the solid state.

3.2 Dimer

In the ground state, two planar monomers form a stacked slided dimer. The intermolecular Au–Au distances are reduced upon excitation and the parallelism of the monomers is broken. The OH and NH groups move out of the monomer planes. The structural differences between the equilibrium structures of the singlet and triplet excited states of the dimer are larger than for the monomer. The optimized ground and excited state structures of

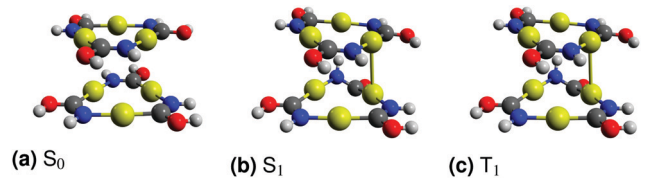

Fig. 4 The molecular structures of the lowest electronic states of the $[Au(HN{=}COH)]_3$ dimer. H in white, C in grey, N in blue, O in red and Au in yellow. The graphics were created using Avogadro.[65,66]

Table 5 Transition energies in cm^{-1} (eV) of the S_0, S_1 and T_1 states of the $[Au(HN{=}COH)]_3$ dimer at the respective equilibrium geometries of the excited state calculated at the TD-DFT, CC2 and XMCQDPT2 levels

Structure	Transition	TD-DFT	CC2	XMCQDPT2
S_0	$S_0 \rightarrow S_1$	32 089 (3.979)	36 225 (4.491)	32 150 (3.986)
S_1	$S_1 \rightarrow S_0$	23 981 (2.973)	27 414 (3.399)	25 931 (3.215)
T_1	$T_1 \rightarrow S_0$	13 202 (1.637)	14 745 (1.828)	16 507 (2.047)

The peak maximum of the solvoluminescence emission band between 510 and 620 nm is at 552 nm, which corresponds to 18 100 cm^{-1} or 2.25 eV.[26]

the $[Au(HN{=}COH)]_3$ dimer shown in Fig. 4 were obtained by using the staggered structure as initial structure. Excitation energies for different molecular structures of the dimer calculated at the TD-DFT, CC2 and XMCQDPT2 levels are reported in Table 5.

The Stokes shift of the S_1 state of about 1 eV between absorption and fluorescence is much smaller than for the monomer. The de-excitation energies of the S_1 and T_1 states as well as the difference between them are larger than in the case of the monomer. A large amount of vibrational relaxation is therefore necessary for the ISC process from S_1 to T_1 due to the large difference between the singlet and triplet de-excitation energies. The difference between the singlet and triplet excitation energies calculated using the S_1 geometry is small. At the B3-LYP, CC2, and XMCQDPT2 levels they are only 0.102, 0.090, and 0.038 eV, respectively. Thus, structural relaxation leads to the large energy difference between S_1 and T_1. The large structural differences between S_0 and T_1 result in a very large Stokes shift of more than 2.3 eV between absorption and phosphorescence, which is also observed experimentally for $[Au(MeN{=}COMe)]_3$. Experimentally, $[Au(MeN{=}COMe)]_3$ absorbs at 230 nm and 300 nm, while the emission occurs between 400 nm and 450 nm.[18,26,32] The same emission can also be assigned to the molecule-like orange-red component of the solid-state emission, which has been explained by the de-excitation of dimer subunits in the solid state that also exhibits a large Stokes shift.[18] The calculated excitation energy of the $[Au(HN{=}COH)]_3$ dimer fits well into the experimental absorption energy range of $[Au(MeN{=}COMe)]_3$. The triplet emission energy is too small compared to the one measured for $[Au(MeN{=}COMe)]_3$. Calculations have shown that the higher emission energies can be reproduced when studying $[Au(MeN{=}COMe)]_3$ instead of the $[Au(HN{=}COH)]_3$ model compound.[37] A direct comparison of the calculated dimer emission energies and the experimental emission spectrum may be difficult due to complexities of aggregate emission.[80]

Photophysical properties of the dimer have been calculated at different levels of theory. The calculated oscillator strengths, spin–orbit coupling matrix elements, and phosphorescence lifetimes at their respective level of theory are listed in Table 6. The rate constants of the radiative and non-radiative transitions were calculated using CC2 and XMCQDPT2 transition energies. The phosphorescence lifetime was calculated only at the CC2 level. The obtained rate constants are summarized in Table 7.

The oscillator strength of the de-excitation from S_1 to S_0 is an order of magnitude larger than for the monomer leading to a

Table 6 Oscillator strength ($f(S_1 \rightarrow S_0)$), spin–orbit coupling matrix elements ($\langle S_1|\hat{H}_{SO}|T_1\rangle$ and $\langle T_1|\hat{H}_{SO}|S_0\rangle$) and phosphorescence lifetime (τ) of the [Au(HN═COH)]$_3$ dimer calculated at the given levels of theory

$f(S_1 \rightarrow S_0)$		$\langle S_1\|\hat{H}_{SO}\|T_1\rangle$	$\langle T_1\|\hat{H}_{SO}\|S_0\rangle$	τ
CC2	XMCQDPT2	CAS-SCF	CAS-SCF	CC2
0.02	0.04	0.27 cm^{-1}	1.6 cm^{-1}	0.19 s

Table 7 The rate constants of the fluorescence (k_r) and phosphorescence (k_{phos}) transitions as well as the rate constants of the non-radiative transitions (k_{IC} and k_{ISC}) between the lowest singlet (S_0 and S_1) and triplet (T_1) states of the [Au(HN═COH)]$_3$ dimer calculated at the CC2 and XMCQDPT2 levels of theory

Level	k_r	k_{IC}	k_{ISC}	k_{phos}
$S_1 \rightarrow S_0$				
CC2	1×10^7 s^{-1}	5×10^{-4} s^{-1}		
XMCQDPT2	2×10^7 s^{-1}	1×10^{-1} s^{-1}		
$S_1 \rightarrow T_1$				
CC2			5×10^6 s^{-1}	
XMCQDPT2			5×10^7 s^{-1}	
$T_1 \rightarrow S_0$				
CC2		0 s^{-1}	0 s^{-1}	5 s^{-1}
XMCQDPT2		0 s^{-1}	0 s^{-1}	—

Table 8 Triplet and phosphorescence quantum yields ϕ_T and ϕ_{phos} of the [Au(HN═COH)]$_3$ dimer calculated at the CC2 and XMCQDPT2 levels

Level	ϕ_T	ϕ_{phos}
CC2	0.33	1.00
XMCQDPT2	0.71	1.00

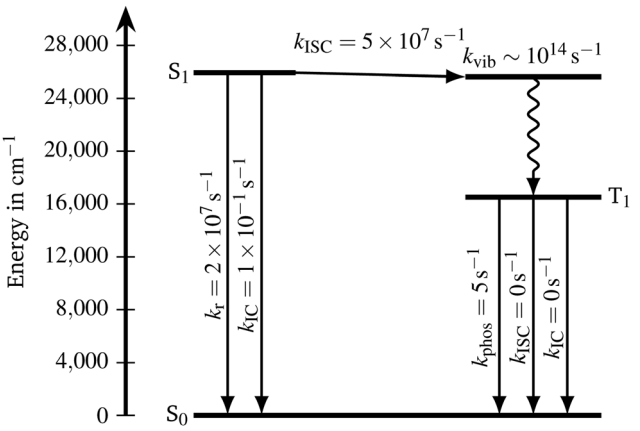

Fig. 5 The Jablonski diagram of the [Au(HN═COH)]$_3$ dimer calculated at the XMCQDPT2 level.

higher fluorescence rate, which makes fluorescence the main competing process to the ISC from S_1 to T_1. The spin–orbit couplings between the ground state, the lowest excited singlet state and the lowest triplet state of the dimer are much smaller than for the monomer. Therefore, the ISC and the phosphorescence processes of the dimer are slower than for the monomer. The ISC process from S_1 to T_1 is still much faster than the IC process and slightly faster than the fluorescence due to the small transition energy for the S_1 structure. The significant differences between the excited state structures leads to strong vibronic coupling of the vibrational modes, which results in a high yield of the triplet state at the XMCQDPT2 level. The IC rate from S_1 is slow due to the small Franck–Condon factors and the large energy of the $S_1 \rightarrow S_0$ transition. The small Franck–Condon factors can be explained by the strong intermolecular aurophilic interactions that lead to dimer formation. The out-of-plane vibrational modes are sterically hindered in the dimer preventing vibrational relaxation through these modes. The constraints on the vibrational modes also affect the IC and ISC processes of the T_1 state. The IC and ISC rates are therefore insignificant for the $T_1 \rightarrow S_0$ transition leading to unity phosphorescence quantum yield. An increased quantum yield has been attributed to small Franck–Condon factors in the past.[81]

For the dimer, there are significant differences between the rate constants calculated using the CC2 and XMCQDPT2 transition energies. The IC and ISC rate constants from S_1 are larger at the XMCQDPT2 level, because the de-excitation energy of the S_1 state is smaller than obtained in the CC2 calculations. The XMCQDPT2 triplet quantum yield is therefore much higher than obtained at the CC2 level. The fluorescence rate from the S_1 state is also faster at the XMCQDPT2 level, because the oscillator strength is twice as large as the value calculated with CC2. The calculated triplet and phosphorescence quantum yields are reported in Table 8. The rate constants calculated at the XMCQDPT2 level are summarized in the Jablonski diagram in Fig. 5.

The dimer displays long lifetime phosphorescence with unity quantum yield and may therefore be the species responsible for the solvoluminescent properties of [Au(MeN═COMe)]$_3$. Thus, when dissolving [Au(MeN═COMe)]$_3$ crystals, the excited state transfers from the solid state to the dimer in solution leading to a long-lived phosphorescent emission that is visible by the naked eye.[26,32,37] The fact that the intensity increases in good solvents of [Au(MeN═COMe)]$_3$ further supports this notion.[33] There is a large difference between the triplet quantum yields calculated using the two methods. The high phosphorescence quantum yield of the [Au(MeN═COMe)]$_3$ dimer could validate further investigations of the [Au(RN═COR′)]$_3$ group of compounds as potential candidates for down-conversion phosphors and as dopants for PhOLEDs. The relaxation of the excited states of the dimer is dominated by the radiative channels. Depending on the employed method, 30% to 70% of the generated singlet states lead to fluorescence on the violet side of the visible spectrum, while the rest of the excited state relaxation happens through phosphorescence on the orange-red side of the spectrum. Triplet and singlet excited states are obtained in a ratio of 3 to 1, when they are created through charge injection. Therefore, a high triplet quantum yield is not as important as the unity phosphorescence quantum yield for PhOLED applications. In the solid state of [Au(MeN═COMe)]$_3$, the orange-yellow phosphorescence band resulting from dimer subunits within the solid state structure and the blue band resulting from the solid state band gap

combine leading to white light emission.[18] The high efficiency of the dimeric emission could qualify this compound for the use in solid-state lighting systems.

4 Conclusion

Rate constants for internal conversion (IC) and intersystem crossing (ISC) have been calculated within the Herzberg–Teller approximation using *ab initio* methods. The relaxation pathway of the lowest excited singlet state is obtained by comparing calculated rate constants of the IC and ISC processes to the calculated rate constants for the fluorescence and phosphorescence emission. The calculations also show how energy differences and Franck–Condon factors affect the relaxation pathway of the lowest singlet state.

The calculation of radiative and non-radiative transition rates of the $[Au(HN{=}COH)]_3$ monomer showed that this compound is not suitable for optoelectronic applications, because non-radiative transitions are the dominating decay channels of the lowest excited states. The calculated emission energies are also very low compared to the experimental luminescence energies of $[Au(MeN{=}COMe)]_3$. The higher experimental de-excitation energies can be explained by dimer formation due to intermolecular aurophilic interactions. Another indication that the dimer might be the emissive species is the experimentally observed large Stokes shift that is also obtained in the phosphorescence calculation for the dimer of the model system but not for the monomer. The $[Au(HN{=}COH)]_3$ dimer has a high triplet and phosphorescence quantum yield at a wavelength of about 600 nm. The long phosphorescence lifetime can explain the yellow solvoluminescence of $[Au(MeN{=}COMe)]_3$ that has been observed in good solvents after irradiation of the crystals with UV light. The photophysical properties of the model system dimer make the $[Au(RN{=}COR')]_3$ dimer and its oligomers potential candidates as dopants for PhOLEDs and as down-conversion phosphors in solid state lighting applications.

Conflicts of interest

There are no conflicts to declare.

Acknowledgements

This work has been supported by the Academy of Finland through projects 314821 and 325369, the Swedish Cultural Foundation in Finland, and Magnus Ehrnrooth Foundation. J. G. thanks the ERASMUS+ SMP program for financial support. The CSC – the Finnish IT Center for Science and the Finnish Grid and Cloud Infrastructure (persistent identifier urn:nbn:fi:research-infras-2016072533) are acknowledged for computer time.

References

1 H. Schmidbaur, *Gold Bull.*, 1990, **23**, 11–21.
2 P. Pyykkö, *Angew. Chem., Int. Ed.*, 2004, **43**, 4412–4456.
3 H. Schmidbaur and A. Schier, *Chem. Soc. Rev.*, 2012, **41**, 370–412.
4 F. Scherbaum, A. Grohmann, B. Huber, C. Krüger and H. Schmidbaur, *Angew. Chem., Int. Ed. Engl.*, 1988, **27**, 1544–1546.
5 H. H. Murray, R. G. Raptis and J. P. Fackler, *Inorg. Chem.*, 1988, **27**, 26–33.
6 C. King, J. C. Wang, M. N. I. Khan and J. P. Fackler, *Inorg. Chem.*, 1989, **28**, 2145–2149.
7 V. W.-W. Yam and K. K.-W. Lo, *Chem. Soc. Rev.*, 1999, **28**, 323–334.
8 E. J. Fernández, M. C. Gimeno, A. Laguna, J. M. L. de Luzuriaga, M. Monge, P. Pyykkö and D. Sundholm, *J. Am. Chem. Soc.*, 2000, **122**, 7287–7293.
9 Q.-M. Wang, Y.-A. Lee, O. Crespo, J. Deaton, C. Tang, H. J. Gysling, M. C. Gimeno, C. Larraz, M. D. Villacampa, A. Laguna and R. Eisenberg, *J. Am. Chem. Soc.*, 2004, **126**, 9488–9489.
10 K. M.-C. Wong, X. Zhu, L.-L. Hung, N. Zhu, V. W.-W. Yam and H.-S. Kwok, *Chem. Commun.*, 2005, 2906.
11 F. Mendizabal, D. Reyes and C. Olea-Azar, *Int. J. Quantum Chem.*, 2005, **106**, 906–912.
12 A. Kishimura, T. Yamashita and T. Aida, *J. Am. Chem. Soc.*, 2005, **127**, 179–183.
13 C. Yang, M. Messerschmidt, P. Coppens and M. A. Omary, *Inorg. Chem.*, 2006, **45**, 6592–6594.
14 S. M. Tekarli, T. R. Cundari and M. A. Omary, *J. Am. Chem. Soc.*, 2008, **130**, 1669–1675.
15 M. Rodríguez-Castillo, M. Monge, J. M. L. de Luzuriaga, M. E. Olmos, A. Laguna and F. Mendizabal, *Comput. Theor. Chem.*, 2011, **965**, 163–167.
16 D. Burgos, C. Olea-Azar and F. Mendizabal, *J. Mol. Model.*, 2011, **18**, 2021–2029.
17 F. Mendizabal and R. Salazar, *J. Mol. Model.*, 2012, **19**, 1973–1979.
18 R. N. McDougald, B. Chilukuri, H. Jia, M. R. Perez, H. Rabaâ, X. Wang, V. N. Nesterov, T. R. Cundari, B. E. Gnade and M. A. Omary, *Inorg. Chem.*, 2014, **53**, 7485–7499.
19 Y. Jiang, S. Alvarez and R. Hoffmann, *Inorg. Chem.*, 1985, **24**, 749–757.
20 P. Pyykkö and Y. Zhao, *Angew. Chem., Int. Ed. Engl.*, 1991, **30**, 604–605.
21 P. Pyykkö and F. Mendizabal, *Inorg. Chem.*, 1998, **37**, 3018–3025.
22 H. Schmidbaur, W. Graf and G. Müller, *Angew. Chem., Int. Ed. Engl.*, 1988, **27**, 417–419.
23 A. L. Balch, E. Y. Fung and M. M. Olmstead, *J. Am. Chem. Soc.*, 1990, **112**, 5181–5186.
24 D. E. Harwell, M. D. Mortimer, C. B. Knobler, F. A. L. Anet and M. F. Hawthorne, *J. Am. Chem. Soc.*, 1996, **118**, 2679–2685.
25 J. Zank, A. Schier and H. Schmidbaur, *J. Chem. Soc., Dalton Trans.*, 1998, 323–324.
26 J. C. Vickery, M. M. Olmstead, E. Y. Fung and A. L. Balch, *Angew. Chem., Int. Ed. Engl.*, 1997, **36**, 1179–1181.
27 R. L. White-Morris, M. M. Olmstead, F. Jiang, D. S. Tinti and A. L. Balch, *J. Am. Chem. Soc.*, 2002, **124**, 2327–2336.

28 R. L. White-Morris, M. M. Olmstead, S. Attar and A. L. Balch, *Inorg. Chem.*, 2005, **44**, 5021–5029.
29 F. Mendizabal, B. Aguilera and C. Olea-Azar, *Chem. Phys. Lett.*, 2007, **447**, 345–351.
30 L. Zhu, V. Coropceanu, Y. Yi, B. Chilukuri, T. R. Cundari and J.-L. Brédas, *J. Phys. Chem. Lett.*, 2013, **4**, 2186–2189.
31 G. Minghetti and F. Bonati, *Inorg. Chem.*, 1974, **13**, 1600–1602.
32 E. Y. Fung, M. M. Olmstead, J. C. Vickery and A. L. Balch, *Coord. Chem. Rev.*, 1998, **171**, 151–159.
33 M. M. Olmstead, F. Jiang, S. Attar and A. L. Balch, *J. Am. Chem. Soc.*, 2001, **123**, 3260–3267.
34 K. Winkler, M. Wysocka-Żołopa, K. Rećko, L. Dobrzyński, J. C. Vickery and A. L. Balch, *Inorg. Chem.*, 2009, **48**, 1551–1558.
35 F. Mendizabal, *Int. J. Quantum Chem.*, 2009, 1279–1286.
36 A. Muñoz-Castro, D. M.-L. Carey and R. Arratia-Pérez, *Chem. Phys. Lett.*, 2009, **474**, 290–293.
37 H. Rabaâ, M. A. Omary, S. Taubert and D. Sundholm, *Inorg. Chem.*, 2017, **57**, 718–730.
38 Y. Sun, N. C. Giebink, H. Kanno, B. Ma, M. E. Thompson and S. R. Forrest, *Nature*, 2006, **440**, 908–912.
39 J. McKittrick and L. E. Shea-Rohwer, *J. Am. Ceram. Soc.*, 2014, **97**, 1327–1352.
40 M. A. Baldo, M. E. Thompson and S. R. Forrest, *Nature*, 2000, **403**, 750–753.
41 D. Escudero, *Chem. Sci.*, 2016, **7**, 1262–1267.
42 X. Zhang, D. Jacquemin, Q. Peng, Z. Shuai and D. Escudero, *J. Phys. Chem. C*, 2018, **122**, 6340–6347.
43 R. R. Valiev, V. N. Cherepanov, G. V. Baryshnikov and D. Sundholm, *Phys. Chem. Chem. Phys.*, 2018, **20**, 6121–6133.
44 R. R. Valiev, V. N. Cherepanov, R. T. Nasibullin, D. Sundholm and T. Kurten, *Phys. Chem. Chem. Phys.*, 2019, **21**, 18495–18500.
45 S. J. Strickler and R. A. Berg, *J. Chem. Phys.*, 1962, **37**, 814–822.
46 B. Helmich-Paris, C. Hättig and C. van Wüllen, *J. Chem. Theory Comput.*, 2016, **12**, 1892–1904.
47 V. Y. Artyukhov, O. K. Bazyl and G. V. Maier, *J. Appl. Spectrosc.*, 2006, **73**, 841–845.
48 R. R. Valiev, V. N. Cherepanov, V. Y. Artyukhov and D. Sundholm, *Phys. Chem. Chem. Phys.*, 2012, **14**, 11508.
49 TURBOMOLE V7.4 2019, a development of University of Karlsruhe and Forschungszentrum Karlsruhe GmbH, 1989-2007, TURBOMOLE GmbH, since 2007; available from http://www.turbomole.com.
50 R. Ahlrichs, M. Bär, M. Häser, H. Horn and C. Kölmel, *Chem. Phys. Lett.*, 1989, **162**, 165–169.
51 O. Treutler and R. Ahlrichs, *J. Chem. Phys.*, 1995, **102**, 346–354.
52 F. Furche, R. Ahlrichs, C. Hättig, W. Klopper, M. Sierka and F. Weigend, *Wiley Interdiscip. Rev.: Comput. Mol. Sci.*, 2013, **4**, 91–100.
53 F. Weigend, M. Häser, H. Patzelt and R. Ahlrichs, *Chem. Phys. Lett.*, 1998, **294**, 143–152.
54 F. Weigend and R. Ahlrichs, *Phys. Chem. Chem. Phys.*, 2005, **7**, 3297–3305.
55 A. D. Becke, *Phys. Rev. A: At., Mol., Opt. Phys.*, 1988, **38**, 3098–3100.
56 C. Lee, W. Yang and R. G. Parr, *Phys. Rev. B: Condens. Matter Mater. Phys.*, 1988, **37**, 785–789.
57 A. D. Becke, *J. Chem. Phys.*, 1993, **98**, 5648–5652.
58 K. Eichkorn, F. Weigend, O. Treutler and R. Ahlrichs, *Theor. Chem. Acc.*, 1997, **97**, 119–124.
59 D. Andrae, U. Häußermann, M. Dolg, H. Stoll and H. Preuß, *Theor. Chim. Acta*, 1990, **77**, 123–141.
60 S. Grimme, S. Ehrlich and L. Goerigk, *J. Comput. Chem.*, 2011, **32**, 1456–1465.
61 M. Casida and M. Huix-Rotllant, *Annu. Rev. Phys. Chem.*, 2012, **63**, 287–323.
62 R. Bauernschmitt and R. Ahlrichs, *Chem. Phys. Lett.*, 1996, **256**, 454–464.
63 F. Furche and R. Ahlrichs, *J. Chem. Phys.*, 2002, **117**, 7433–7447.
64 D. Rappoport and F. Furche, in *Theoretical and Computational Chemistry*, ed. M. Olivucci, Elsevier Science, 2005, ch. III, vol. 16.
65 Avogadro: an open-source molecular builder and visualization tool. Version 1.2.0. http://avogadro.cc/.
66 M. D. Hanwell, D. E. Curtis, D. C. Lonie, T. Vandermeersch, E. Zurek and G. R. Hutchison, *J. Cheminform.*, 2012, **4**, 17.
67 P. Deglmann, F. Furche and R. Ahlrichs, *Chem. Phys. Lett.*, 2002, **362**, 511–518.
68 P. Deglmann and F. Furche, *J. Chem. Phys.*, 2002, **117**, 9535–9538.
69 C. Hättig and F. Weigend, *J. Chem. Phys.*, 2000, **113**, 5154.
70 C. Hättig and K. Hald, *Phys. Chem. Chem. Phys.*, 2002, **4**, 2111–2118.
71 A. A. Granovsky, *J. Chem. Phys.*, 2011, **134**, 214113.
72 Alex A. Granovsky, Firefly version 8, http://classic.chem.msu.su/gran/firefly/index.html.
73 R. Send and F. Furche, *J. Chem. Phys.*, 2010, **132**, 044107.
74 D. G. Fedorov, S. Koseki, M. W. Schmidt and M. S. Gordon, *Int. Rev. Phys. Chem.*, 2003, **22**, 551–592.
75 M. W. Schmidt, K. K. Baldridge, J. A. Boatz, S. T. Elbert, M. S. Gordon, J. H. Jensen, S. Koseki, N. Matsunaga, K. A. Nguyen, S. Su, T. L. Windus, M. Dupuis and J. A. Montgomery, *J. Comput. Chem.*, 1993, **14**, 1347–1363.
76 M. S. Gordon and M. W. Schmidt, *Theory and Applications of Computational Chemistry*, Elsevier, 2005, pp. 1167–1189.
77 G. Herzberg and E. Teller, *Z. Phys. Chem.*, 1933, **21B**, 410–446.
78 M. R. Silva-Junior, M. Schreiber, S. P. A. Sauer and W. Thiel, *J. Chem. Phys.*, 2008, **129**, 104103.
79 M. Schreiber, M. R. Silva-Junior, S. P. A. Sauer and W. Thiel, *J. Chem. Phys.*, 2008, **128**, 134110.
80 N. J. Hestand and F. C. Spano, *Chem. Rev.*, 2018, **118**, 7069–7163.
81 W. Cai, A. Zhao, K. Ren, R. He, M. Li and W. Shen, *J. Phys. Chem. C*, 2019, **123**, 17968–17975.